Journal of Materials Chemistry A

Accepted Manuscript

Volume 4 | Number 1 | 7 January 2016 | Pages 1–330

Journal of
Materials Chemistry A

Materials for energy and sustainability
www.rsc.org/MaterialsA

ISSN 2050-7488

ROYAL SOCIETY OF CHEMISTRY

PAPER
Kun Chang, Zhaorong Chang et al.
Bubble-template-assisted synthesis of hollow fullerene-like MoS₂ nanocages as a lithium ion battery anode material

175 YEARS

ROYAL SOCIETY OF CHEMISTRY

rsc.li/materials-a

Journal Name

ARTICLE

Triple Phase Boundary Augmentation in Hierarchical, Pt grafted N-doped Mesoporous Carbon Nanofibers for High Performance and Durable PEM Fuel Cells

Karthikeyan K Karuppanan,[a] Appu V Raghu,[a] Manoj Kumar Panthalingal,[b] Sivasubramanian Ramanathan,[a,c] Thanarajan Kumaresan[d] and Biji Pullithadathil,*[a,c]

Pt electrocatalysts grafted, hierarchical mesoporous carbon nanofibers (Pt/MPCNFs) have been developed using electrospinning for high performance PEM fuel cells. The morphological analysis of Pt/MPCNFs revealed uniformly dispersed Pt nanoparticles (2-3 nm) strongly grafted on the hierarchical nanochannels of mesoporous carbon nanofibers (MPCNFs). The pyridinic and pyrrolic nitrogens formed in the sp^2 graphitic structure during the carbonization process of the MPCNFs have found to play a major role in augumentation of triple phase boundaries in the catalyst support materials. Pt/MPCNFs exhibited outstanding electrocatalytic performance towards oxygen reduction reaction (ORR) with positively shifted onset potential (54 mV), half-wave potential (78 mV) and high limiting current density (4.75 mA/cm^2 at 0.4 V) than the state-of-the-art Pt/C electrocatalysts in acidic medium and exhibited superior long-term stability (89.8 % retention after 30000 s and less change in activity after 10,000 potential sweeps). Pt/MPCNFs as cathode catalyst yielded maximum power density of 428.6 mW/cm^2 during single cell testing, which is 2.08 times higher than commercial Pt/C electrocatalyst. The electrochemical performance evaluation clearly implied that the unique combination of ultrathin nanofibers with three-dimensional mesoporous structure, high electrical conductivity, enhanced specific surface area, homogeneous dispersion of Pt nanocatalysts and the presence of optimal nitrogen doping offers superior electrocatalytic activity *via* favorable four-electron pathway and long-term operating stability during repeated cycles. Performance analysis in single PEM fuel cell shows twice the power density (428 mW/cm^2) with Pt/MPCNFs compared to commercial electrocatalyst membranes due to the effective enhancement in triple phase boundaries, indicating Pt/MPCNFs as a potential candidate for high performance, durable PEMFCs.

1. Introduction

The increasing depletion of fossil fuels and environmental pollution continue to increase the global demand for alternative sustainable and clean (zero by-product emission) energy. The proton exchange membrane fuel cells (PEMFCs) show great contribution in energy research owing to its advantages, such as high power density, low pollution and low operating temperature[1–5]. Typical PEMFC comprises of electrodes (catalyst layer of Pt or Pt-alloy nanomaterials supported on carbon-based nanostructure material) and a separating polymer electrolyte membrane. During last few

decades, several research ideas have been explored in order to achieve better catalyst efficiency in polymer electrolyte membrane fuel cells by developing new support materials and catalyst particles[1–3,6]. The major reduction in the performance of fuel cells is observed mainly due to an inadequate utilization of nanoparticles in the catalyst layer. The triple-phase boundary (TPB) (where, the catalyst particles are in contact with ionomers, support material and gas pores for accomplishing the electrochemical reaction) play vital role in the enhancement of efficiency and solely depends on the proper utilization of the catalyst particles and porous texture of the support material. Therefore, a large TPB length is crucial for improving the electrochemical performance of PEM fuel cells[7–11].

Nanostructured carbon support materials are considered to be an ideal candidate for PEM fuel cells owing to their synergic characteristics, such as high specific surface area, electrical conductivity, physical/chemical stability and adequate water management capacity besides their high surface area and low-cost. Though, carbon black is extensively used as the support for the Pt catalyst (specific surface area 250 m^{2}g^{-1}), recent reports manifested that few undesirable properties of carbon black, such as dense structure (smaller pore size affect the contact between Nafion ionomers and the catalyst particles), agglomeration of

a. Nanosensor Laboratory, PSG Institute of Advanced Studies, Coimbatore, 641004, INDIA.
b. Department of Mechanical Engineering, PSG Institute of Technology and Applied Research, Coimbatore- 641 062, INDIA
c. Department of Chemistry, PSG College of Technology, Coimbatore-641004, INDIA
d. Department of Automobile engineering, PSG college of technology, Coimbatore-641004, INDIA

* Corresponding author E-mail: bijuja123@yahoo.co.in

ARTICLE

nanoparticles, corrosion and surface chemistry diminishes the electrocatalytic activity[12–15]. In the recent years, lots of carbon-based nanostructured materials, such as nanotubes, OMCs, graphene, aerogels, nanofibers, boron doped diamond, nanocoils, carbon nanohorns and hollow graphitic spheres have been proposed as catalyst supports for PEMFCs in order to maximize the utilization of nanocatalyst[16–26]. Among these materials, carbon nanofibers (CNFs) have been well addressed in PEMFC applications due to its unique properties, such as one-dimensional structure, high specific surface area, superior electrical conductivity, high mechanical strength, thermal and electrochemical stability[27–33].

It has been well accepted that carbonaceous nanofibers with porous structure demonstrate an improved performance in catalysis, sensors and electronic devices [34,35]. The presence of micropores (<2 nm) in the support material trapped the metallic nanoparticles and makes them inaccessible to electrochemical reaction which adversely affects the triple phase boundary leading to the loss of Pt utilization[36]. For instance, conventional carbon support materials have more micropores (< 2 nm) and deep cracks hinders the formation of TPB and decreased the utilization of catalyst as it is difficult for proton conducting electrolyte and reactants to access the micropores. Similarly, the carbon supports with macropores (> 50 nm) posses less surface area and poor electrical conductivity. Hence, it is anticipated that the efficiency of the carbon supported catalyst depends on both structure and size of the pores as well as the electrical conductivity of mesoporous carbon materials[37,38]. Recent studies demonstrated that the porous carbon support materials having a mesopore size of ~25 nm exhibited the highest performance compared to commercially available catalyst [39,40]. Briefly, the mesoporous structure with high specific surface area, optimal pore sizes (2 -50 nm) and large pore volumes are highly desirable for the deposition of metal nanoparticles and smooth diffusion of reactants and product species[414243]. Till now, several reports on mesoporous carbons materials with graphitic pore walls are demonstrated for their remarkable performance towards applications, such as, fuel cells, lithium storage, lithium-ion batteries electrode materials, catalyst supports and adsorbents [33,41,44,45]. Recently, mesoporous one-dimensional materials are gaining more attention towards fuel cell applications [25,33,46–53]. A series of efforts have been devoted to overcome the challenges involved in controlled synthesis and characterization of Pt catalysts supported CNFs for PEMFCs and DMFCs. However, a methodical approach for obtaining mesoporous carbon nanofiber supports to achieve high electrochemical activity toward oxygen reduction reaction for PEMFCs has not been thoroughly investigated so far.

Electrospinning technique is identified as one of the most convenient and effective method to prepare carbon nanofibers. Typically, carbon nanofibers (CNFs) made from electrospun polyacrylonitrile (PAN) nanofibers have gained wider interest for energy applications due to their high electrical conductivity, good mechanical properties, high surface area, lightweight, low cost, scalability and excellent flexibility[54–57]. In order to achieve effective catalyst utilization in fuel cells, a proper support material must be developed which improves the active triple phase boundaries. In order to attain high dispersion, proper utilization, activity and stability of the catalyst particles, support materials should have large specific surface area, uniform pore size, interconnected hierarchical pore network, good electrical conductivity and mechanical stability which would be more desirable for the improvement of reaction kinetics during fuel cell operations. Recently, we have reported the development of mesoporous carbon nanofibers from PAN/NaHCO$_3$ nanocomposite nanofibers using electrospinning followed by the thermally induced selective phase removal mechanism[58].

Herein, we report the development of Platinum nanocatalysts grafted N-doped hierarchical mesoporous carbon nanofibers as a highly active, durable electrocatalyst material with enhanced TPB sites and its performance analysis towards PEM fuel cells. The electrochemical properties of electrocatalysts Pt/CNFs, Pt/MPCNFs and commercially available carbon blacks were compared through ORR studies. Presence of mesoporous structure and the presence of pyridinic and pyrrolic nitrogen doping in the carbon nanofibers were identified to be responsible for higher specific activity for oxygen reduction reaction than those of commercial Pt/C and carbon nanofiber supported catalysts. Pt/MPCNFs based electrocatalyst exhibited significant high PEMFC performance owing to its superior electrochemical surface area and enhanced mass transport due to the presence of micro and mesoporous network in nanofibers, which facilitated the accessibility of the O$_2$ molecules and ions with Pt electrocatalytic sites minimizing the diffusion path length for ORR reaction.

2. Experimental Section

2.1 Materials and Methods

Polyacrylonitrile (PAN, average molecular weight = 150 000), hexachloroplatinic acid (H$_2$PtCl$_6$.6H$_2$O, Aldrich), N-dimethylformamide (DMF, 99%, Merck), Sodium bicarbonate (NaHCO$_3$, 99.9%, Merck), ethylene glycol (EG, Merck), isopropanol (IPA, Merck), sulphuric acid (H$_2$SO$_4$, Merck) and nitric acid (HNO$_3$, Merck) were used for the preparation of Pt@MPCNFs. The commercial catalyst Vulcan XC-72 (20 wt % Pt on carbon, Cabot Corp.), 5% Nafion ® 117 solution in low aliphatic alcohols and Nafion® 117 membrane (Dupont Industries), carbon papers (Toray) were used for fabrication of fuel cell catalyst layer. All reagents were of analytical grade and directly used without any further purification.

2.2 Preparation of Mesoporous carbon Nanofibers

Mesoporous carbon nanofibers (MPCNFs) were prepared according to our previous work[58]. In brief, 7 % w/v PAN and PAN (7% w/v)/ball milled NaHCO$_3$ nanoparticle (1% w/v) solution in DMF were prepared with vigorous stirring for 2 h at 60° C. The PAN/NaHCO$_3$ solution was further subjected to ultrasonication process for 15 min to enable proper dispersion. The electrospinning of PAN and PAN/NaHCO$_3$ was carried out to prepare PAN and PAN/NaHCO$_3$ nanocomposite nanofibers. The optimized electrospinning parameters such as, solution feed rate (0.5 mL/h), applied voltage (30 kV), needle-to-collector distance (30 cm) and needle diameter (21 G) were used throughout the process. The fiber was deposited on a clean copper sheet (7x7 cm) for 5 h to produce a thick nanofibrous mat. The as-spun PAN and PAN/NaHCO$_3$ nanocomposite nanofibers were subjected to

subsequent two-step thermal treatment process consisting of stabilization (290° C) and carbonization (800° C) in air and nitrogen with a ramping rate of 5° C/min, respectively, to obtain porous carbon nanofibers and carbon nanofibers.

2.3 Functionalization of Mesoporous carbon nanofibers

The conventional carbon nanofibers and porous carbon nanofibers samples were functionalized using an acid treatment of H_2SO_4 (3 M) and HNO_3 (3 M) (3:1 v/v) under reflux conditions. The CNFs and MPCNFs samples were vigorously refluxed with H_2SO_4-HNO_3 mixture at 120 °C for 8 h. At the end of the reaction, the resultant samples were washed several times with distilled water until the neutral P^H was attained, filtered and dried overnight in a vacuum oven at 120°C.

2.4 Pt catalyst loading on CNFs and MPCNFs

The Pt electrocatalyst (20 wt %) supported on CNFs and MPCNFs were synthesized by an ethylene glycol (EG) reduction method [29,59,60]. Briefly, 20 mg of functionalized carbon nanofibers based support material was dispersed in 50 mL of ethylene glycol and a calculated amount of chloroplatinic acid was slowly dropped into the suspension, followed by stirring for 30 mins at room temperature. The pH was adjusted to 13.0 by addition of 2.5 M NaOH solution. The dispersion was heated up to 130 °C and refluxed 130 °C for 3h under nitrogen atmosphere. The slurry was filtered, thoroughly washed several times with ethanol and dried in vacuum oven at 80°C to obtain 20% Pt catalyst loaded carbon nanofibers and mesoporous carbon nanofibers. Carbon nanofibers, mesoporous carbon nanofibers, Pt incorporated carbon nanofibers, and Pt incorporated mesoporous carbon nanofibers are denoted as CNFs, MPCNFs, Pt/CNFs and Pt/MPCNFs, respectively.

2.5 Fabrication of Membrane Electrode Assembly and Single Cell Testing

In order to make the hydrophobic gas diffusion layer, the carbon paper was pre-treated with 30 % PTFE solution. In order to prepare a homogeneous electrocatalyst ink, required amount of 20% of electrocatalysts, such as Pt/MPCNFs, Pt/CNFs and commercial Pt/C were dispersed in a mixture of isopropanol, ultrapure water and Nafion® ionomer solution (5 wt%) and ultrasonicated for 30 mins. The slurry was then spray coated onto the gas diffusion layer (carbon paper) and dried at 80°C for 30 min. The total loading of the platinum electrocatalyst of both the anode and cathode was controlled as 0.3 mg/cm² in all the samples. The pretreated Nafion® 117 membrane was sandwiched between the prepared electrodes with an active area of 5x5 cm² and hot bonded at 10 MPa and 130°C to prepare membrane electrode assembly (MEA). The fabricated MEAs were assembled between two graphite plates with a grooved flow channels for gas flow. The humidified hydrogen and oxygen reactant gases were supplied to maintain the water level in membrane. The humidifying temperature of hydrogen and oxygen was maintained at 40°C. The flow rate of the hydrogen and oxygen gases was 400 and 200 ml/min, respectively. Prior to record the polarization curve, the electrodes were activated. The polarization curves were obtained from single cell testing using a fuel cell test station (Biologic FCT-50S).

2.6 Characterization Techniques

The X-ray diffraction (XRD) patterns were collected using Cu–Kα radiation (λ=1.5406 Å) with a powder X-ray diffractometer (Panalytical X-pert) to identify the crystal structures of the prepared materials. The working voltage and current was 40 kV and 30 mA, respectively. The patterns were acquired between 10° and 90° 2θ. The micro structural parameters were analyzed using JCPDS software. Morphology, size, distribution and crystallinity of the various support material samples were characterized by high-resolution transmission electron microscope (HRTEM, JEOL JEM 2100, Japan). The prepared samples were coated on a carbon film supported by a 200-mesh copper grid. The measurements were carried out with an accelerating voltage of 200 keV. The attenuated total reflectance Fourier-transform infrared (ATR-FTIR) analysis was carried out on an IR Affinity series 1S (Shimadzu, Japan) in the spectral ranges from 4500 to 400 cm^{-1} with a resolution of 2 cm^{-1} to elucidate the functional group of carbonized and functionalized nanofibers. BET analysis was investigated using nitrogen absorption/desorption isotherms obtained on an Autosorb-1 apparatus (Quantachrome, Florida, USA) at 77 K after degassing at 200°C and the corresponding surface areas were determined based on the Brunauer-Emmett-Teller (BET) equation and pore size distributions were determined by Non local density functional theory (NLDFT) method. Synthesized and modified nanofibrous mats (1x1 cm) were subjected to electrical conductivity measurement via electrometer (Keithely Instruments, model-SMU-2420, USA) using a four-probe method at room temperature under ambient conditions. The surface elemental analysis and chemical bonding state of the various electrocatalysts were performed using X-ray photoelectron spectroscopy (Thermoscientific, k-Alpha) with a monochromatic Al Kα (hυ = 1486.6 eV) radiation source with a charge neutralizer. Wide energy survey scans were obtained with a binding energy range of 0–1360 eV, pass energy of 150 eV, and an energy step of 1 eV. The high resolution spectral data were acquired from the circular spot size, pass energy and step size were 400 μm, 30 eV and 0.1 eV, respectively.

2.7 Electrochemical characterization

The electrochemical performance measurements of Pt catalysts supported on MPCNFs, CNFs and commercial Vulcan Pt/C were carried out on an electrochemical work station (CH instruments (CHI600E, USA)) in 0.5 M H_2SO_4. The electrochemical performance was evaluated by cyclic voltammetry (CV), along with linear sweep voltammetry (LSV) under ambient temperature. The experiments were performed using a typical three-electrode cell with a polished glassy carbon (GC) working electrode (geometrical area: 0.007 cm²) and GC RDE (geometric area: 0.0314 cm²) for CV and LSV studies. The working electrode was prepared with a Nafion bonded films (20% Pt/CNFs and Pt/MPCNFs) on GCE. A Pt wire and Ag/AgCl were served as a counter electrode and reference electrode (all the potentials were reported versus reversible hydrogen electrode (RHE)), respectively. Similarly, the RDE experiments were performed with various rotating rates and a scan rate of 10 mV/s. The working electrode was prepared by modifying glassy carbon (GC) electrode. GC electrode was pre-cleaned by polishing with 0.3 and 0.05 μm alumina slurries to achieve a mirror-like surface, followed by washing and ultrasonicating with water and acetone. The samples of electrocatalyst loaded on porous carbon nanofibers

were fabricated on the glassy carbon electrode using a drop of 0.1% solution of Nafion and the coating was further dried at room temperature. Similarly, CNFs and commercial catalysts (20 wt% Pt/C (Vulcan XC-72)/ethanol/Nafion mixture) were also investigated for comparison. In order to acquire reproducible and consistent results, freshly prepared electrolyte (0.5 M H_2SO_4) were used for each measurement. High pure nitrogen and oxygen were bubbled through the electrolyte solution for 30 min to create nitrogen and oxygen atmosphere near to the working electrode.

3. Results and discussion

3.1 Synthesis of Pt decorated MPCNFs

Figure 1 schematically illustrates the synthetic process adopted for the preparation of Pt/MPCNFs. Our previous report has established the successful synthesis of mesoporous carbon nanofibers from the blend of PAN/NaHCO$_3$ nanocomposite nanofibers[58]. The prepared carbon nanofiber surfaces are generally smooth and chemically inert and hence it is necessary to activate the graphitic surface which is contributing to the uniform dispersion and size control of the catalyst particles. The carbon nanofibers were pretreated to introduce the hydrophilic groups (–COOH, -C=O and –OH) for effective anchoring of the Pt nanocatalyst (Figure 1). The texture and surface chemistry of prepared mesoporous carbon nanofibers were modified by harsh acidic treatment to expand their ability to disperse metal nanoparticles. The presence of mesoporous structure in the porous carbon nanofibers contributes to the penetration of acids throughout the fibers which paves the way to increase additional active sites compared to conventional carbon nanofibers. Further, the functionalized carbon nanofiber mats were immersed into the chloroplatinic acid solution to adhere Pt^{2+} ions on the surface of nanofibers. Upon the introduction of Pt^{2+} ions, the functional groups (C-O-H) on the surface of CNFs make synergetic interactions with metal ions (C-O-Pt) through an ion exchange or coordination reaction and serve as nucleation centers[31,61]. Then Pt^{2+} ions were further reduced to Pt (0) using ethylene glycol reduction which produced a well dispersed Pt nanoparticles having controlled size on the modified surface of carbon nanofibers. Interestingly, compared to regular CNFs, the MPCNFs were found to have well distributed and smaller sized Pt nanoparticles. The large surface area and the combination of micro/mesopores can effectively improve the deposition of Pt nanocatalyst particles when they are employed as supports. In addition, the controlled size of the mesoporous structure in the nanofiber provides more accessible areas to the contact of electrolyte, supported catalyst particles and gas molecules (triple phase boundaries).
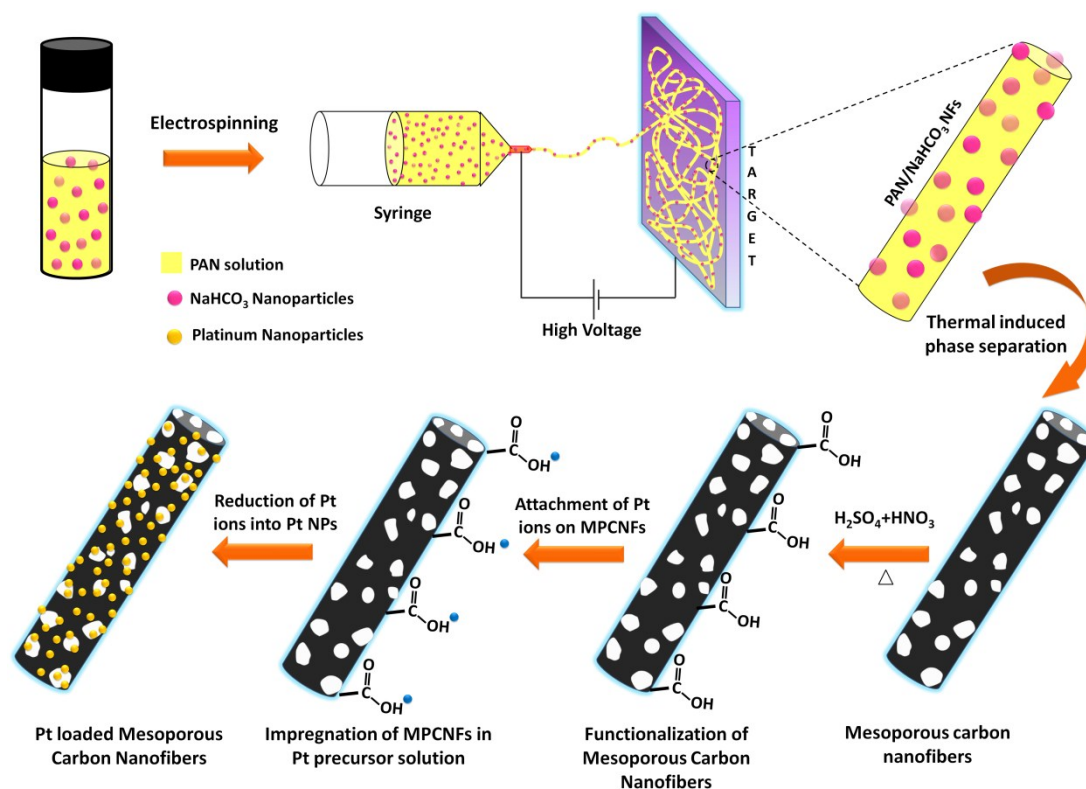
Figure 1. Schematic representation of deposition of Pt nanoparticles on mesoporous carbon nanofiber supports.

3.2. X-ray diffraction Analysis

The small angle XRD patterns elucidate the phase composition and crystallographic properties of the prepared electrocatalysts are shown in Figure 2. All samples exhibited a typical broad peak located between 25° and 45°, which is ascribed to the diffraction of (002) and (101) planes of hexagonal graphite structure of the carbon support[58]. According to JCPDS database (87-0646), the main resolved diffraction patterns of the Pt/CNFs and Pt/MPCNFs can be identified at 2θ= 39.5, 46.3, 67.7, 81.9 and 85.6, which are attributed to the crystal planes (111), (200), (220), (311) and (222) of face-centered cubic (fcc) crystal structure of metallic platinum.

Moreover, platinum oxides or hydroxide peaks have not appeared in the XRD patterns. The average crystallite size (d) of the Pt nanoparticles could be calculated from the Pt (111) peak according to the Debye-Scherrer formula (1),

$$d = 0.9\lambda/(\beta \cos\theta) \quad .... \quad (1)$$

Where, λ is the X-ray wavelength (Cu Kα, λ=0.154 nm), β and θ are the full width at half maximum of the peak intensity (FWHM) in radians and the Bragg angle, respectively. The average crystallite size of the Pt nanoparticles was calculated to be 6.8 nm for Pt/CNFs and 2 nm for Pt/MPCNFs, respectively. The structure and properties of the mesoporous carbon nanofibers have significant impact on the size and distribution of Pt nanoparticles. The smaller size and narrow distribution of the Pt nanoparticles are attributed to the large number of defective sites (edge atoms of pyridinic and pyrrolic type nitrogen species as revealed from XPS analysis) present in MPCNFs. Generally, more number of pyridinic nitrogen atoms tends to locate at the edges of the graphitic layers. The presence of abundant mesopores leads to the formation of greater number of pyridinic and pyrrolic type nitrogen species at the edges of the broken graphitic layers and the Pt nuclei readily attach at these sites during in-situ ethylene glycol reduction. These nitrogen species enhance the Pt adsorption on the CNFs surface due to its large electron affinity[62]. In addition, presence of large number pyridinic nitrogen disrupts the planar hexagonal arrangement of carbon atoms in MPCNFs leading to the formation of rough surface. Pt prefers to nucleate at these kinks on the MPCNFs surfaces, where the pyridinic nitrogen atoms are located[63] resulting in smaller size distribution (~2 nm) compared to CNFs (~6.8 nm). More detailed structural characterization of MPCNFs is reported in our previous studies[58].
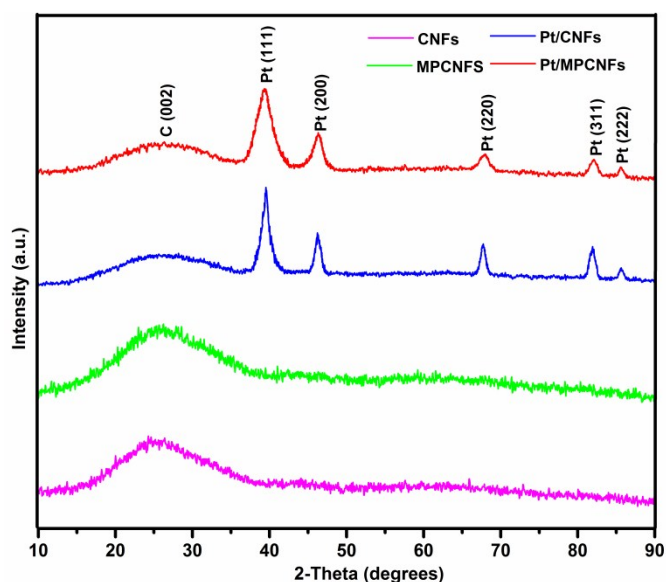

Figure 2. XRD patterns of CNFs, MPCNFs, Pt/CNFs and Pt/MPCNFs.

3.3 Transmission Electron Microscopic Analysis

HRTEM analysis was performed to investigate the surface morphology, dispersion of Pt nanoparticles and also for understanding the crystallinity of CNFs, MPCNFs and platinum nanoparticle loaded CNFs and MPCNFs. Fig.3 (a-b) depicts the

typical porous morphology of the porous carbon nanofibers resulted from the carbonization of as-spun PAN/NaHCO$_3$ composite nanofibers under inert atmosphere, in accordance with our previous report[58]. Supporting information, Figure S1 (a-d) displays the TEM images of the pristine carbon nanofibers prepared from PAN nanofibers and platinum nanoparticles loaded CNFs having a homogeneous diameter (~160 nm) and smooth surface with micropores (< 2 nm). Moreover, Pt/CNFs exhibits that the catalyst is not firmly attached and distributed on CNFs surface and as a result an uneven deposition of the particles with prevalent agglomeration have appeared. The rough surface of porous carbon nanofibers prepared from PAN/NaHCO$_3$ nanocomposite nanofibers is mainly caused by the evolution of numerous identical pores in intra-fibers which is due to the complete removal of NaHCO$_3$ nanoparticles.

These fibers exhibit an average diameter of ~ 130 nm with uniform mesopore size in the range of 20-50 nm, which can expose more active sites for the uniform deposition and distribution of Pt nanoparticles. It is already reported that the distribution and size reduction of catalyst nanoparticles are greatly influenced by the existence of mesopores in the nanofibers[64]. As evident from TEM analysis, the MPCNFs possess many mesopores, defected and rough surface that might expose more active sites during the process of Pt catalyst preparation, which improves the interaction of Pt nanoparticles leading to uniform distribution of Pt nanoparticles without aggregation [65,66]. It is understood that the reduction in particle size can be attributed to increase in mesopore formation on the surface of the nanofibers. Fig. 3 (c-d) indicate the uniform distribution of the catalyst particles having spherical morphology on the support material and inset shows the average diameter of Pt particles in the range of 2-3 nm, estimated by counting over 300 particles at different regions of the nanofibers using Image J software. The size of the Pt nanoparticles calculated from TEM images was found to be consistent with the size observed from XRD patterns. High-resolution TEM (HRTEM) (Fig 3d) prominently disclosed that the porosity of MPCNFs and CNFs belonged to typical randomly distributed mesopores and micropores respectively. The selected area diffraction (SAED) pattern shows the polycrystalline nature of Pt nanoparticles. The SAED pattern (Fig 3e) reveals that the nanocrystalline structure of Pt nanoparticles and their planes also were matching with the XRD planes. Moreover, the distinctive porous structure and uniform distribution of catalyst particles in the matrix additionally provided a large space to adsorb the reactant molecules which can enhance the interaction with ionomers and electrocatalyst (Triple phase boundary). The presences of the unique mesopore structures in the carbon nanofibers can be more favorable for the penetration of electrolyte. The lattice fringe of metallic Pt nanoparticles marked in the high-resolution image (Fig 3g) was measured to be 0.229 nm which is in good agreement with the d-spacing values measured from JCPDS database (87-0646).

ARTICLE

Journal Name
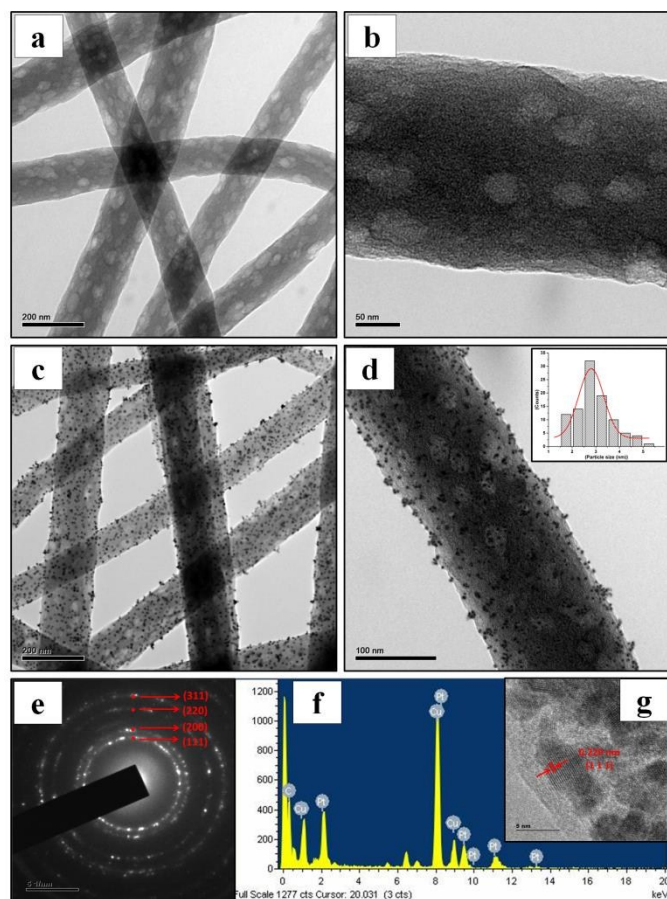
Figure 3. (a-b)TEM images of MPCNFs, (c-d) Pt/MPCNFs (inset: histogram), (e-f) selected area electron diffraction (SAED) pattern, elemental analysis of Pt/MPCNFs and (g) high resolution image.

3.4 Fourier Transform Infrared spectroscopic analysis

The attenuated total reflection Fourier-transform infrared spectrum of the functionalized carbon nanofibers are depicted in Figure S2 (see supporting information) in order to elucidate the chemical structure. After acidic treatment (H_2SO_4/HNO_3 at 120°C for 8 h) of CNFs and MPCNFs, the formation of $-SO_3OH$, $-COOH$ and $-OH$ groups on the surface of the nanofibers were evidenced. The presence of sulfonic acid groups was confirmed from the characteristic peak appeared at 1365 cm^{-1}. The peaks at 1715 and 1658 cm^{-1} can be assigned to the presence of carbonyl groups in ester and ring structure. The most important features are the stretching and bending mode vibration of $-COOH$ which were confirmed by the spectral bands situated at 1095 cm^{-1} and 950 cm^{-1}, respectively. A broad band located at 3441 cm^{-1} is attributed to the characteristic O-H stretching frequency of the hydroxyl group which can be ascribed to the oscillation of carboxylic groups (O=C-OH and C-OH). The peak appearing at 2631 cm^{-1} is associated with O-H stretching of strongly bonded carboxylic group. The results imply that both CNFs and MPCNFs exhibit similar spectra revealing the formation of surface functional groups corresponding to the oxidation of carbon nanofibers which is in agreement with previous reports[29,67]. The formation of functional groups on the peripheral walls of carbon nanofibers would further contribute to the dispersion of Pt nanoclusters.

3.5 BET Analysis

Figure 4 shows the N_2 adsorption-desorption isotherms and pore size distribution curves of the as-synthesized CNFs, MPCNFs and catalyst loaded CNFs/MPCNFs. The parameters derived from BET surface area analysis are summarized in Table 1. The adsorption-desorption isotherm of CNFs and Pt/CNFs was found to be Type 1 according to the IUPAC classification demonstrating their microporous structure. But, the MPCNFs and Pt/MPCNFs exhibited a combination of I/IV type isotherms with H_4 hysteresis loops, the multilayer adsorption at low-pressure region and the capillary condensation occurred at a relative pressure in the range of 0.6-0.9 which revealed the co-existence of micro/mesoporous texture. The formation of mesopores was mainly due to the removal of the $NaHCO_3$ nanoparticles in CNFs. As a result, the surface area and total pore volumes of the MPCNFs and Pt/MPCNFs were found to be predominantly increased compared to CNFs and Pt/CNFs which is due to the increase in the large number of defects[42]. The inset in Figure 4 displays the corresponding pore size distribution (PSD) derived from non-local density functional theory (NLDFT) method. The pore size distribution of Pt/MPCNFs demonstrating one sharp peak at 2 nm and a broad peak at 20-50 nm reveal the characteristics of microporous and mesoporous structures, respectively. The estimated pore size of Pt catalyst supported MPCNF and CNFs are 12.6 and 1.32 nm, respectively. The pore size distribution of Pt/MPCNFs was found to be slightly reduced as compared to bare carbon nanofibers because of the deposition of the Pt catalyst particles. But still, the PSD curves and H_4 hysteresis loops (rapid raise in nitrogen adsorption occurred at high-pressure region) of MPCNFs and Pt loaded MPCNFs proved that it possess micropores and large number of mesopores. However, the Pt supported on MPCNFs possesses much greater total pore volume as compared to Pt/CNFs. Therefore, this co-existence of micro/meso 3D texture, high specific surface area, high pore volume are liable to increase the uniform distribution of electrocatalyst and thereby increase the active catalytic sites, ionomers contact and fuel diffusivity to achieve enhanced electrochemical performance[25].
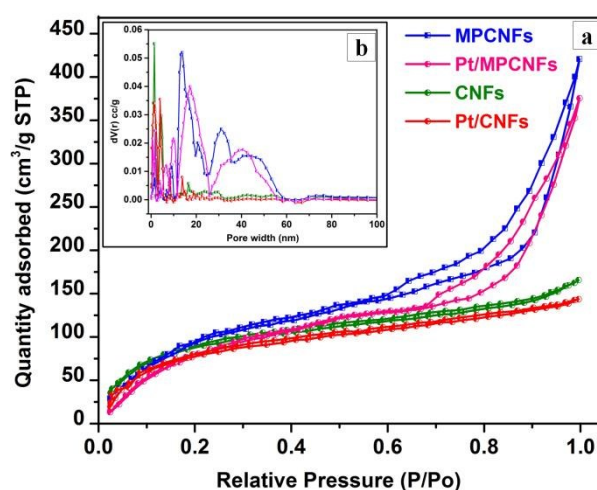
Figure 4. Nitrogen adsorption/desorption isotherms (a) and corresponding NLDFT pore size distribution curves (b) of CNFs, MPCNFs, Pt/CNFs and Pt/MPCNFs.

Table 1. Textural characteristic of CNFs, MPCNFs, Pt/CNFs and Pt/MPCNFs

| Sample	S_{BET} (m^{2}g^{-1})[a]	TPV (cm^{3}g^{-1})[b]	V_{micro} (cm^{3}g^{-1})[c]	V_{meso} (cm^{3}g^{-1})[d]	APD (nm)[e]
CNFs	150	0.318	0.26	0.06	1.40
Pt/CNFs	143	0.298	0.23	0.06	1.32
MPCNFs	724	0.710	0.44	0.27	13.8
Pt/MPCNFs	685	0.592	0.38	0.21	12.6

[a] S_{BET}- BET surface area; [b] TPV- total pore volume; [c] V_{micro}- micropore volume; [d] V_{meso}- mesopore volume; [e] APD- average pore diameter

3.6 X-ray photoelectron spectroscopy

In order to elucidate the elemental composition and chemical oxidation states of surface species, X-ray photoelectron spectroscopy (XPS) analysis was performed. As shown in Figure 5-6, the XPS survey spectra of both Pt/CNFs and Pt/MPCNFs display four predominant peaks at 284, 531, 399, and 72 eV corresponding to C1s, O1s, N1s and Pt4f corroborating the presence of elements, such as carbon, oxygen, nitrogen, and platinum. The high-resolution C1s spectra were further deconvoluted to analyze four species, namely, sp^2 hybridized carbon atom (284.7 eV), ternary alcohols or C-N bond (286.1), C=O (286.7 eV) and COOH (288 eV), respectively. During the formation of carbon nanofibers under high-temperature in inert atmosphere, unstable active free radicals could be formed by losing hydrogen from the carbon chain. Depending on the unstable free radicals in the carbon chain, it readily react with water and oxygen, generating C=O, C-OH, and COOH in the resulting structure. The deconvoluted high-resolution O1s spectra of Pt/CNFs and Pt/MPCNFs indicate the presence of C=O (531.4 eV), C-OH (532.9 eV) and COOH (533.3 eV), which are well agreement with the identifications from N1s and O1s spectra. It is understood that the presence of functional groups in graphitic carbon nanofibers can promote more anchoring and effective dispersion of Pt nanoparticles[68]. Moreover, the percentage of oxygen-containing functionalities is comparatively higher in the case of porous carbon nanofibers which are highly desirable for the catalyst attachment. In general, increasing the nitrogen content in the carbon support material can be more favorable for ORR reaction[69,70]. But, an excessive temperature can deteriorate nitrogen content in the graphitic structure. As illustrated in Figure 5d and 6d, the deconvoluted N1s spectra of carbon nanofibers indicate the presence of four types of nitrogen bonding states in the support material, such as pyridinic nitrogen (398.3 eV), pyrrolic nitrogen (400 eV), quaternary nitrogen (401.2 eV) and pyridinic-N-oxide (403 eV). The percentage of nitrogen species was estimated from the integral areas of these peaks as demonstrated in Figure 5f and 6f.

The porous carbon nanofibers exhibited comparatively higher percentage of pyridinic nitrogen species than carbon nanofibers and it is believed to result from the occurrence of more abundant micro/mesopores in the nanofibers structure. The pyridinic and pyrrolic type nitrogen species are known to reduce the charge transport resistance and impart high electrocatalytic properties as the nitrogen atom possessed planer sp^2 hybridization which would not disrupt the π- π conjugation in graphitic carbon nanofibers. Moreover, the carbon atoms adjacent to pyridinic and pyrrolic N can be activated, where oxygen molecules are adsorbed and reduced during ORR[71]. It is noteworthy that the resultant products are nitrogen-doped carbon nanofibers particularly with pyridinic and pyrrolic nitrogen species are more suitable for ORR reaction [72]. At the same time, increase in temperature causes reduction in doped nitrogen species which may not be favorable for ORR. As summarized in Table 2, the pyridinic nitrogen content is higher in Pt/MPCNFs electrocatalyst, compared to Pt/CNFs suggesting that the nitrogen edge atoms in the carbon chains can increase current density and boost electrocatalytic reactions. A high-resolution spectrum of Pt 4f was found to be emerged as a doublet peak with a 4f$_{7/2}$:4f$_{5/2}$ intensity ratio of 4:3, which is originated from the spin-orbital coupling of 4f photoelectron transitions. In addition to this, the non-symmetrical peaks of Pt 4f orbital suggest the presence of more than one oxidation state. Hence, these peaks were further deconvoluted and fitted into four peak signals. According to literature, the lowest binding energy components associated with the most intense peaks at 71.9 and 74.7 eV can be attributed to zero valent metallic state platinum nanoparticles. The second pair of higher binding energy peaks appearing at 72.5 and 75.9 eV are assigned to platinum oxide and hydroxides namely, PtO/PtO$_2$ and Pt(OH)$_2$. It is clearly observed that the metallic state of platinum and oxidized states of platinum in Pt/MPCNFs support were approximately 74.2 % and 25.8 % of the total intensity of platinum. It is worth mentioning that Pt (0) is more active than other species and the noticed relative percentage of Pt (0) in Pt/MPCNFs (74.2 %) is higher than that of Pt/CNFs (70.8 %), as summarized in Table 2.
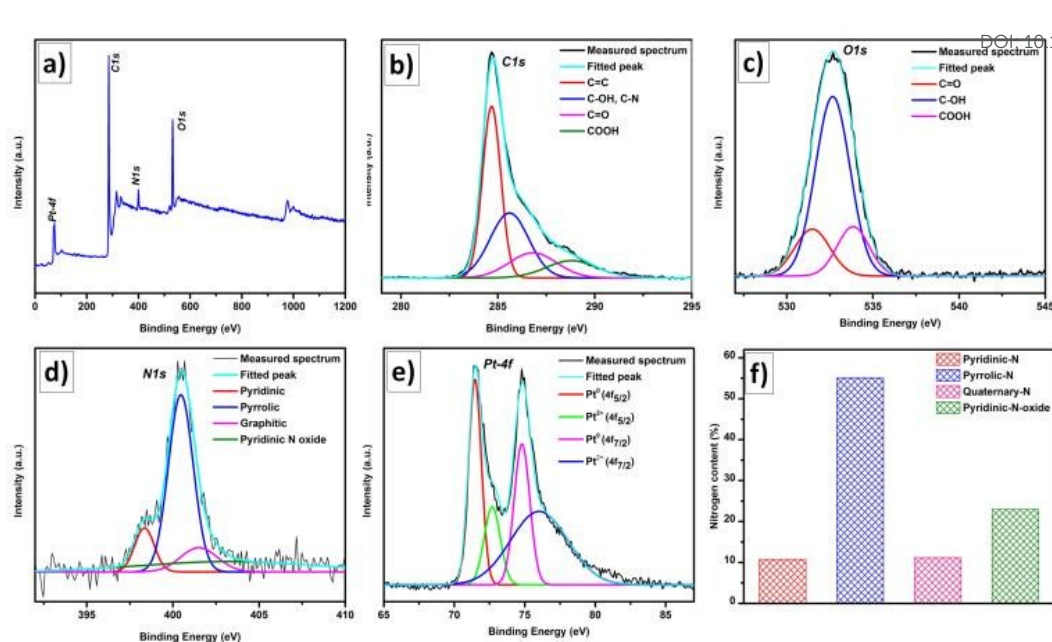
Figure 5. XPS spectra analysis for of Pt/CNFs (a) survey scan, (b) C1s, (c) O1s, (d) N1s, (e) Pt4f and (f) the percentage of nitrogen content as calculated from N1s spectra.
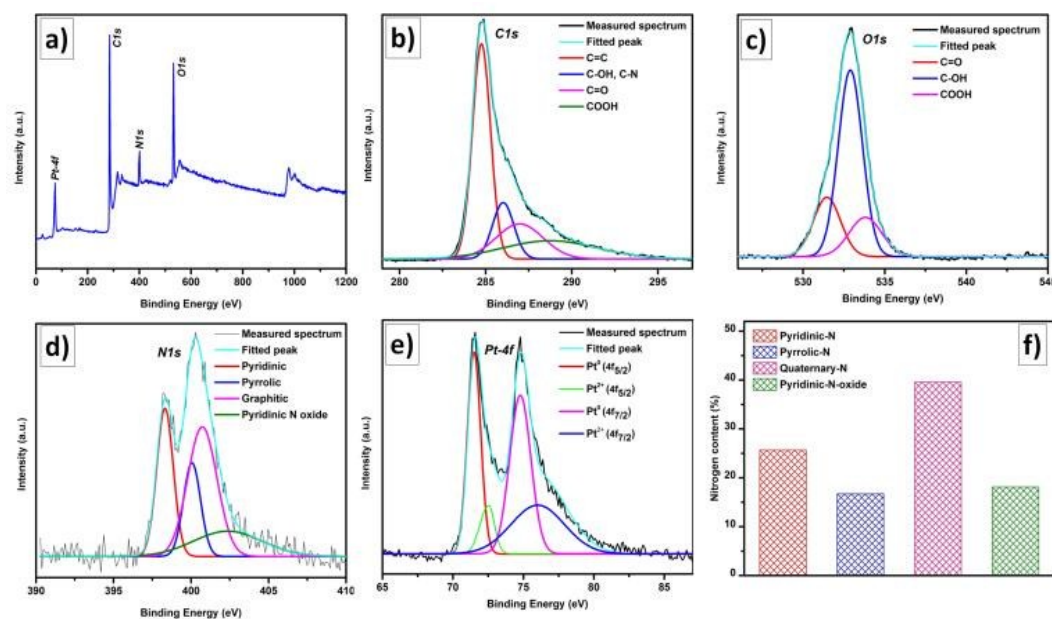
Figure 6. XPS spectra analysis of Pt/MPCNFs (a) survey scan, (b) C1s, (c) O1s, (d) N1s, (e) Pt4f and (f) the percentage of nitrogen content as calculated from N1s spectra.

Table 2. The relative surface atomic concentration of C, N, O, Pt and nitrogen distributions.

Catalyst	Atomic weight (at %)				Nitrogen content (%)			
	C	N	O	Pt	Pyridinic-N	Pyrrolic-N	Graphitic- N	Pyridinic-N-oxide
Pt/CNFs	77.8	3.73	16.2	1.54	10.7	55.1	11.2	22.9
Pt/MPCNFs	72.2	8.79	16.9	2.04	25.6	16.7	39.5	18.1

3.7 Electrical Conductivity Measurement

The electrical conductivity of carbonaceous material plays a vital role in achieving high performance in fuel cell applications[73]. I-V

characteristics of CNFs, MPCNFs, f-CNFs, f-MPCNFs, f-Pt/CNFs and f-Pt/MPCNFs carried out (Supporting information, Figure S3) at room temperature to elucidate the electrical conductivity properties. The electrical conductivity of CNFs, MPCNFs, f-CNFs, f-MPCNFs, Pt/CNFs, and Pt/MPCNFs were 323, 293, 310, 283, 330 and 337 S/m respectively. The electrical conductivity of the porous carbon nanofibers (293 S/m) was found to be slightly decreased compared to CNFs (323 S/m) which was due to the evolution of pores in the nanofibers. Moreover, the electrical conductivity in both CNFs and MPCNFs was further reduced after functionalization compared to bare carbon nanofibers due to the structural disorders occurred during the oxidation process. Although the electrical conductivity of the f-MPCNFs (283 S/m) was found to be lesser compared to f-CNFs (310 S/m), it was further increased after the integration of nanoparticles onto the peripheral walls of the nanofibers. The highest electrical conductivity was achieved in the case of Pt/MPCNFs, as expected due to the uniformly distributed Pt nanoparticles over the support material enhancing the transport properties of the electrons across the graphitic layers.

3.8 Electrocatalytic activity

Several reports have demonstrated that the mesoporous containing carbon nanostructures exhibited high electrocatalytic activity towards methanol oxidation reaction and oxygen reduction reactions[26,74,75]. In this investigation, the electrochemical performance and stability of Pt electrocatalyst supported on mesoporous carbon nanofibers are studied. Figure 7a shows the cyclic voltamograms of the commercial Pt/C, Pt/CNFs, and Pt/MPCNFs using N_2 saturated H_2SO_4 (0.5 M) at room temperature between 0 to 1.2 V (Vs RHE) with a sweeping rate of 50 mVs^{-1}. The hydrogen adsorption/desorption peak maxima was obtained between 0.01 and 0.4 V for Pt/MPCNFs which was found to be larger compared to Pt/CNFs and Pt/C. The electrochemical active surface areas (ECSA) of the supported catalysts were calculated from the coloumbic charge of the hydrogen adsorption peak according to the following equation[31,76].

$$ECSA = Q_H / (0.21 \times [Pt]) \dots\dots\dots\dots\dots\dots\dots\dots (1)$$

Where, Q_H is the charge exchange during hydrogen elctroadsorption (mC.cm^{-2}), 0.21 is the charge required for monolayer hydrogen adsorption on the polycrystalline Pt and [Pt] represent the Pt loading on the glassy carbon electrode. Inductively coupled plasma atomic emission spectrometry (ICP-AES) was carried out to estimate the Pt contents in the Pt/MPCNFs, Pt/CNFs, and Pt/C electrocatalysts. The content of platinum (L_{Pt}), calculated electrochemical active surface areas (ECSA), charge exchange of the Pt/MPCNFs, Pt/CNFs and Pt/C are summarized in Table 3. The charge under hydrogen adsorption/desorption was found to be drastically enhanced in the case of Pt/MPCNFs than other support materials. The characteristic reduction peak corresponding to the removal of Pt surface oxides between 1.0 and 0.5 V was observed in all the support materials. Pt/MPCNFs demonstrates excellent hydrogen adsorption and desorption peaks

than Pt/CNFs and Pt/C, that shows a larger ECSA value of 95.3 m^2 g^{-1} compared to 61.1 m^2 g^{-1} and 49.2 m^2 g^{-1} for Pt/CNFs and Pt/C respectively. The enhancement of ECSA of Pt/MPCNFs could be mainly because of the small and well dispersed Pt catalyst anchored on the porous structure of the carbon nanofibers.

Table 3. Summary of electrochemical parameters calculated from CV of Pt/CNFs, Pt/MPCNFs and Pt/C in 0.5 M H_2SO_4.

Sample	L_{Pt} (mg)	Q (μC)	ECSA (m^2/g)
Pt/MPCNFs	0.0192	384.6	95.3
Pt/CNFs	0.0189	252.4	61.1
Pt/C	0.0197	201.7	49.2

L_{Pt}, the amount of Pt loading on glassy carbon electrode; Q, total charge collected in the hydrogen adsorption region; ECSA, electrochemical surface area.

The oxygen reduction reaction (ORR) is one of the most significant reactions in fuel cells which consumes large amount of Pt to be used in PEMFCs in order to achieve high power density. The ORR performance of Pt/MPCNFs in acidic media was evaluated using cyclic voltammetry (CV) in O_2-saturated 0.5 M H_2SO_4 electrolyte at a scan rate of 10 mVS^{-1} and also compared with Pt/CNFs and Pt/C. As shown in Figure 7b, well-defined cathodic reduction peaks centered at about 0.81, 0.83 and 0.86 V for Pt/C, Pt/CNFs and Pt/MPCNFs, respectively, suggesting the excellent electrocatalytic activity of highly porous carbon nanofiber based support materials. Linear sweep voltammograms (LSVs) (Figure 7c) using rotating disk electrode (RDE was also recorded at a rotation speed of 1600 rpm and a sweep rate of 10 mVs^{-1} in order to further understand the electrochemical pathways of oxygen reduction reaction performance of Pt/PCNFs. The ORR performance through LSV results of all catalysts are directly related with the cathodic limiting current density, onset potential and half-wave potentials. From RDE polarization curves, it was noticed that the onset potentials of Pt/MPCNFs, Pt/CNFs and Pt/C appeared at 0.99, 0.98 and 0.93 V, respectively. The half-wave potential of Pt/MPCNFs, Pt/CNFs, and Pt/C are 0.91, 0.88, and 0.83 V and the current densities at 0.4 V were 4.75, 4.47, and 4.04 mAcm^{-2}, respectively. The tremendous ORR activity of Pt/MPCNFs can be deduced from both half-wave potential and onset potential. The electrochemical parameters of the electrocatalyst are compared in Figure 7f and summarized in Table 4. As evident from CV and RDE studies, the PCNF based electrocatalyst exhibited more positive onset potential and half-wave potential ($E_{1/2}$) among all electrocatalysts. Similarly, their current density for oxygen reduction reaction also was higher in the case of Pt/MPCNFs compared to Pt/CNFs and Pt-C. These results indicate that performance enhancement may be because of the unique characteristics, such as increased number of high-density active sites present due to the increased surface area, the existence of controlled size of mesopores, small diameter and exposed edge planes in the nanofibers.
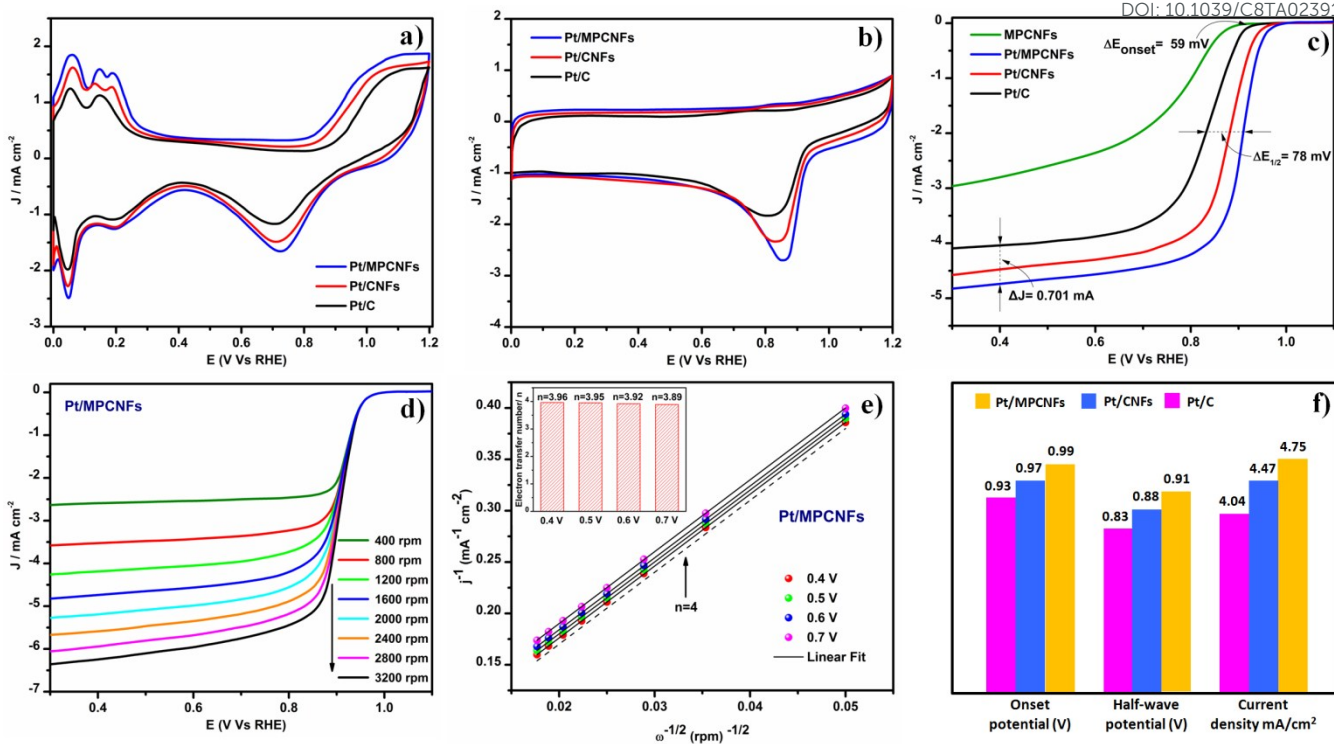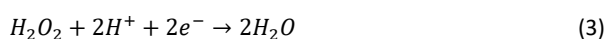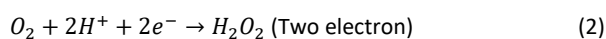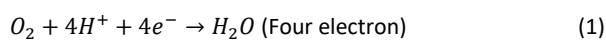
Figure 7. a) Comparison of the electrocatalytic activity of Pt/MPCNFs, Pt/CNFs and commercial 20% Pt/C by cyclic voltammetry in N_2-saturated 0.5 M H_2SO_4 solution with a scan rate of 50 mV s^{-1}, (b) ORR performance of Pt/MPCNFs, Pt/CNFs and commercial 20% Pt/C catalysts in O_2-saturated 0.5 M H_2SO_4 solution with a scan rate of 50 mV s^{-1}. (c) LSV plots obtained from RDE at 1600 rpm for MPCNFs, Pt/MPCNFs, Pt/CNFs and 20% Pt/C in O_2 saturated 0.5 M H_2SO_4 at a scan rate of 10 mV/s. (d) RDE curves of Pt/MPCNFs tested at different rotation rates. (e) Koutecky-Levich plots and the corresponding electron transfer numbers derived from RDE data (inset) of electrocatalysts. (f) Comparison of electrocatalytic parameters obtained from LSV results of the electrocatalyst materials.

Table 4. Electrochemical parameters derived from CV and LSV measurements.

Electrocatalyst	Onset potential (mV)	Limited current density mA/cm^2 (at 0.4 V)	Half wave potential (mV)
Pt/MPCNFs	993	4.75	911
Pt/CNFs	978	4.47	883
Pt/C	934	4.04	834

In order to further demonstrate the mechanism of catalytic activity, LSV curves of Pt/MPCNFs sample was obtained with different rotation rates using RDE technique. It is observed that the oxygen reduction current increases with increasing of rotation rate. Typically, the ORR follows two-electron and four-electron reduction pathways as described in equation (1) and (2, 3) respectively. The four-electron pathway is more favorable for fuel cell reactions. The kinetic parameters at different rotation speeds was carefully investigated based on the Koutecky-Levich (K-L) equation 4 and 5.

$$O_2 + 4H^+ + 4e^- \rightarrow H_2O \text{ (Four electron)} \tag{1}$$

$$O_2 + 2H^+ + 2e^- \rightarrow H_2O_2 \text{ (Two electron)} \tag{2}$$

$$H_2O_2 + 2H^+ + 2e^- \rightarrow 2H_2O \tag{3}$$

$$\frac{1}{J} = \frac{1}{J_k} + \frac{1}{J_d} = -\frac{1}{nFkC_{O_2}^b} - \frac{1}{0.62nFD_{O_2}^{2/3}\nu^{-1/6}C_{O_2}^b\omega^{1/2}} \tag{4}$$

$$B = 0.62nFC_{O_2}(D_{O_2})^{2/3}\nu^{-1/6} \tag{5}$$

Where, n is the number of electrons transferred per oxygen molecule during ORR, F is the Faraday constant (96485 C mol^{-1}), j is the measured current density, j_k and j_d are the kinetic and diffusion limited current densities, respectively; k is the electron transfer rate constant, D_{O_2} is the diffusion coefficient of O_2 in H_2SO_4 (1.8 x 10^{-5} cm^2 s^{-1}), C_{O_2} is the dissolved concentration of O_2 in H_2SO_4 (1.1 x 10^{-6} mol cm^{-3}) and ν is kinematic viscosity of the electrolyte (0.01 cm^2 s^{-1}).

The K-L data of Pt/PCNFs electrocatalyst showed good linearity and parallelism in the selective potential range, manifesting that it follows first-order kinetics. Moreover, Figure 7f exhibited transferred number of electrons of Pt/MPCNFs during oxygen reduction process determined based on Koutecky-Levich plot (Figure 7e). Therefore, it is suggested that the highest near four electron pathways of Pt/MPCNFs exhibit a more efficient electrochemical reduction in acidic media. The high density of catalytic sites in carbon nanofibers contributed in an excellent electrocatalytic activity due to its increase electrolyte/catalyst contact area and more adsorption sites for O_2 molecule during ORR process. Hence, it is concluded that the near four electron transfer pathway and high current density confirms the superior activity of

ORR in acid media. The electrochemical impedance spectroscopy (EIS) was used to infer about the charge transfer resistance (R_{ct}) in order to gain further information about the electrocatalytic activity of ORR. Figure S5 illustrates the Nyquist plots corresponding to the Pt/MPCNFs, Pt/CNFs and Pt/C in a frequency range of 100 kHz to 10 mHz and all of them exhibited characteristic semicircle in high-frequency region and an inclined straight line in the low-frequency region. It is well known that the intercept of the impedance real axis of Nyquist plot represents the resistance of the electrolyte (R_s). At medium frequency, the diameter of the semicircle in the Nyquist plots corresponds to charge transfer resistance characteristics on the electrode (Rct). In the low frequency, the slope of the 45° portion of the Nyquist plots is associated with the Warburg resistance (R_w) and is a result of the frequency dependence of ion diffusion in the electrolyte to the electrode interface.[77–79] However, the diameter of the semicircle was found to be smaller for Pt/MPCNFs electrode in the high-frequency range among all other samples, manifesting that the lowest charge transfer resistance at the electrode/electrolyte interface. In the low-frequency range, a straight line of the Pt/MPCNFs electrode is more vertical in the imaginary part of the impedance as compared to other samples, which means low diffusion resistance of electrolyte ions and increased adsorption/desorption of ions onto the electrode surface. According to Nyquist plots, the Pt/MPCNFs exhibit a lower value of charge transfer resistance (1.6 Ω) than those of Pt/CNFs (2.4 Ω) and Pt/C (2.9 Ω) catalysts, which demonstrated that a good accessibility of the electrolyte ions to the Pt/MPCNFs electrode. This phenomenon implies that the Pt/MPCNFs possess high electronic conductivity as compared to other two catalysts, which could be more beneficial for the improvement of electrocatalytic activity for ORR. According to the above indicated results, this performance enhancement could be explained based on two major aspects; (1)the low electrical resistance in the electrodes was attributed to the more efficient transport of electrons across the graphitic layer in the one-dimensional conductive network of the carbon nanofiber resulting from well distributed Pt nanoparticles in the CNFs, (2) a high surface area with a large mesopore volume provides increased charge transport and short distance ion diffusion pathway.

Therefore, we believe that the higher ORR performance is mainly attributed to the improved electrical conductivity and high surface areas with large mesopore volumes, which satisfy the requirement of electronic continuity for electrocatalyst and easy accessibility of reactant and protons.

3.8.1 Durability Studies

In order to understand the electrochemical stability in acidic environment, an accelerated degradation test (ADT) was performed using a stable current-time (j-t) chronoamperometric response in an oxygen saturated 0.5 M H_2SO_4 at a constant voltage of 0.6 V (Figure 8a). After reaction of 30,000 s, Pt/PCNFs was found to maintain 89.8 % of initial current density, while other reference catalysts such as Pt/CNFs and Pt/C maintained about 83.2 and 65.2 %, respectively. It is evident that the relative current of Pt/MPCNFs electrocatalyst was not largely declined as a function of time, which indicates that the electrochemical activity was retained even after longtime operations. Figure 8 (b-d) displays a series of LSV curves of Pt/MPCNFs, Pt/CNFs and Pt/C recorded after continuous potential cycles for 10,000 times under ambient temperature. The half wave potential $E_{1/2}$ of Pt/PCNFs showed a small negative shift of 21 mV which is significantly lesser than that of Pt/CNFs (36 mV) and Pt/C mV with (79 mV), indicating that Pt/PCNFs based electrocatalyst had much better stability than other two electrocatalysts. Therefore, it is suggested that the excellent durability of Pt/MPCNFs could be attributed due to the presence of mesopores that could keep Pt nanoparticles fixed locally and prevent them from aggregation. The high electrocatalytic activity and better durability of the MPCNFs are attributed to the uniform pore size and open pore edges of the support material which can maximize the contact area for O_2 molecules during oxygen reduction reaction (ORR) process. In addition, the reduced size of the Pt nanoparticles creates a large number of active sites since the catalytic reaction only occurs at the surface of the nanoparticles. The amalgamation of the high specific surface area, smaller sized catalyst nanoparticles, and defected surfaces with mesopores are more favorable for attaining higher electrocatalytic activity towards ORR process.
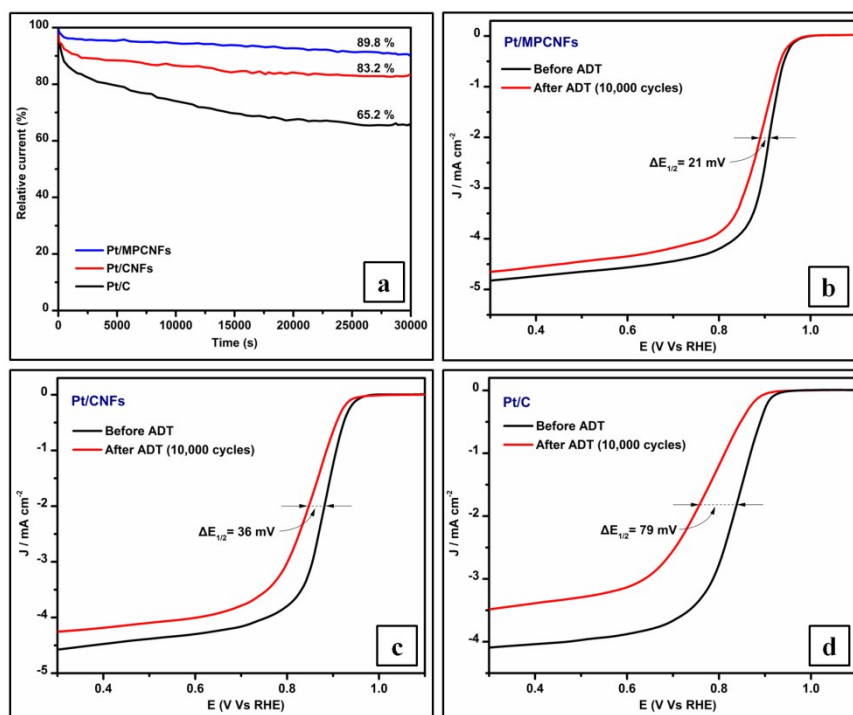
Figure 8. Electrochemical stability measurements from the (a) current–time (j–t) chronoamperometric responses of Pt/MPCNFs, Pt/CNFs and Pt/C for 30,000 s in O_2-saturated 0.5 M H_2SO_4 at a constant potential of 0.6 V and (b-d) LSV curves Pt/MPCNFs, Pt/CNFs and Pt/C on RDE (1600 rpm) before and after 10,000 potential cycles in O_2-saturated 0.5 M H_2SO_4at a scan rate of 10 mV/s.

.

3.9 Single Cell Testing

According to the literature, the electrode performance in membrane electrode assembly (MEA) may differ from half cell tests[80]. Figure 9 showed the polarization (V-J and P-J) curves of H_2-O_2 single PEMFCs with various carbon supports on the cathode side. The MEA with porous carbon nanofibers exhibited best performance compared to Pt/CNFs and commercial Vulcan Pt/C under the same conditions. The maximum current density (J_{max}) obtained for Pt/MPCNFs, Pt/CNFs and commercial Pt/Vulcan carbon are 1114.4, 916.4 and 651.3 mA/cm^2, respectively. The maximum power density value of Pt/MPCNFs (428 mW/cm^2) is 2.08 and 1.44 times higher than Pt/C (205 mW/cm^2) and Pt/CNFs (296 mW/cm^2) respectively. The obtained polarization curve parameters are summarized in Table 5. The results indicated that MPCNFs based support could significantly improve the cell performance, mainly due to the superior electrochemical surface area and enhanced mass transport due to the presence of micro and mesoporous network in one-dimensional nanofibers. In addition to the better utilization of Pt electrocatalyst, the presence of pyridinic and pyrrolic nitrogen content in the support material also enhanced the performance of fuelcell reactions by minimizing the charge transport resistance. It should be addressed that the enhancement

occurs in low current density (activation region) and high current density region (mass transport region) ascribed to the outstanding electrocatalytic activity and decreased mass transport resistance.
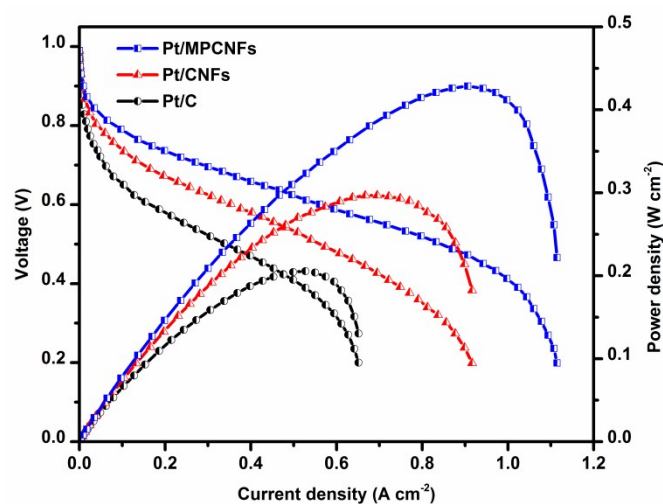
Figure 9. PEM fuelcell performance curves of Pt/CNFs, Pt/MPCNFs and a commercial Vulcan Pt/C electrocatalysts.

Table 5. Polarization curve parameters from single cell performance analysis

Cathode electrocatalysts	OCV (mV)	J_{max} (mA.cm^{-2})	P_{max} (mW.cm^{-2})	Current density (i) at P_{max} (mA.cm^{-2})
Pt/MPCNFs	998	1114.4	428.6	906.2
Pt/CNFs	976	916.4	296.8	694.9
Pt/C	934	651.3	205.5	527.4

Conclusions

The present study reports a new strategy for the rational design and synthesis of Pt/MPCNFs electrocatalyst using electrospinning, thermal treatment followed by impregnation and chemical reduction method. Interestingly, Pt/MPCNFs shows high catalytic activity compared to that of Pt/CNFs and commercial Pt/C catalyst which is due to the high specific surface area (685 m^2/g) and controlled pore size (20-40 nm). In addition, identical size of spherical pores in the MPCNFs makes particle size smaller and uniform. Consequently, Pt electrocatalysts supported on mesoporous carbon nanofibers have shown high electrochemical activity than other carbon-based electrocatalyst material and commercial electrocatalyst material. It is well understood that the superior electrocatalytic activity and highest electrochemical stability is predominantly attributed to the development of more catalytic active sites (triple phase boundaries) because of the smaller and uniformly distributed particle size. Furthermore, the presence of pyridinic and pyrrolic nitrogen content also contributed towards enhancing the performance. The porous carbon nanofiber possessed high effective specific surface area with micro/mesopores facilitated the larger accessibility of the O_2 molecules and ions with the Pt electrocatalytic sites which minimized the diffusion path length for ORR reaction. It is envisaged that these graphitic mesoporous carbon nanofiber structures with well-distributed Pt electrocatalyst can be a promising catalyst support material for fuel cell reactions with potential to replace conventional carbon support materials.

Conflicts of interest

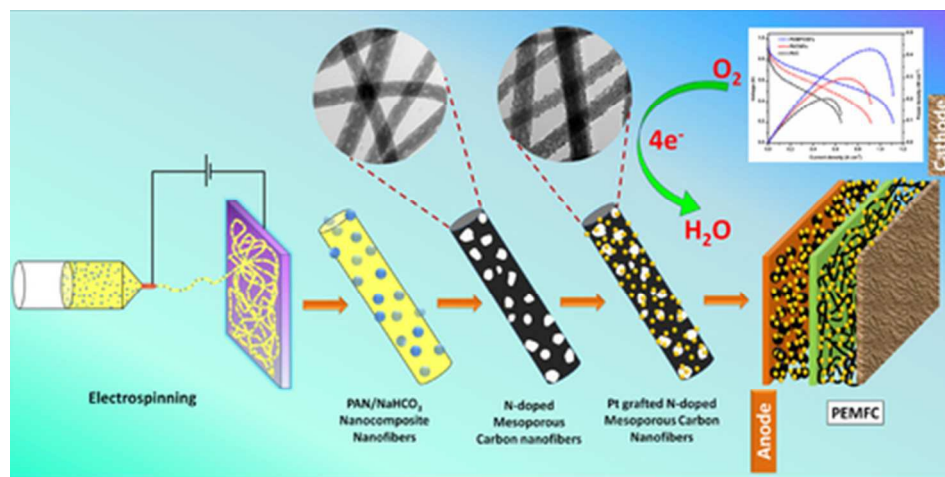The authors declare no conflict of interest.

Acknowledgements

Notes and references

1   N. Jung, D. Y. Chung, J. Ryu, S. J. Yoo and Y. E. Sung, *Nano Today*, 2014, **9**, 433–456.

2   M. Yaldagard, *World J. Nano Sci. Eng.*, 2013, **2013**, 121–153.

3   N. Veizaga, J. Fernandez, M. Bruno, O. Scelza and S. De Miguel, *Int. J. Hydrogen Energy*, 2012, **37**, 17910–17920.

4   P. Zamani, D. Higgins, F. Hassan, G. Jiang, J. Wu, S. Abureden and Z. Chen, *Electrochim. Acta*, 2014, **139**, 111–116.

5   D. C. Higgins and Z. Chen, *Can. J. Chem. Eng.*, 2013, **91**, 1881–1895.

6   H. Huang and X. Wang, *J. Mater. Chem. A*, 2014, **2**, 6266–6291.

7   Y. Su, H. Liu, Z. Yan, M. Feng, J. Tang and H. Du, *Electrochim. Acta*, 2015, **164**, 182–186.

8   S. Martin, Q. Li and J. O. Jensen, *J. Power Sources*, 2015, **293**, 51–56.

9   O. J. Curnick, B. G. Pollet and P. M. Mendes, *RSC Adv.*, 2012, **2**, 8368.

10   R. O'Hayre and F. B. Prinz, *J. Electrochem. Soc.*, 2004, **151**, A756.

11   N. . Brandon and D. . Brett, *Philos. Trans. R. Soc. A Math. Phys. Eng. Sci.*, 2006, **364**, 147–159.

12   Y. Shao, G. Yin, J. Zhang and Y. Gao, *Electrochim. Acta*, 2006, **51**, 5853–5857.

13   Z. Du, H. Zhao, Y. Shen, L. Wang, M. Fang, K. Świerczek and K. Zheng, *J. Mater. Chem. A*, 2014, **2**, 10290–10299.

14   J. C. Meier, C. Galeano, I. Katsounaros, A. A. Topalov, A. Kostka, F. Schu and K. J. J. Mayrhofer, .

15   K. Huang, K. Sasaki, R. R. Adzic and Y. Xing, *J. Mater. Chem.*, 2012, **22**, 16824.

16   S. N. Stamatin, M. Borghei, R. Dhiman, S. Ma, V. Ruiz, E. Kauppinen and E. M. Skou, "*Applied Catal. B, Environ.*, 2015, **162**, 289–299.

17   D. S. Yang, D. Bhattacharjya, M. Y. Song and J. S. Yu, *Carbon N. Y.*, 2014, **67**, 736–743.

18   C. Wang, H. Gao, H. Li, Y. Zhang, B. Huang, J. Zhao, Y. Zhu, W. Z. Yuan and Y. Zhang, *Nanoscale*, 2014, **6**, 1377–83.

19   G.-P. Kim, M. Lee, Y. J. Lee, S. Bae, H. D. Song, I. K. Song and J. Yi, *Electrochim. Acta*, 2016, **193**, 137–144.

20   H.-S. Oh and H. Kim, *Adv. Funct. Mater.*, 2011, **21**, 3954–3960.

21   G. Ren, X. Lu, Y. Li, Y. Zhu, L. Dai and L. Jiang, *ACS Appl. Mater. Interfaces*, 2016, **8**, 4118–4125.

22   J. Kim, Y. Chun, S. Lee and D. Lim, *RSC Adv.*, 2014, **5**, 1103–1108.

23   2015, 2015.

24   H. Wang, Y. Liu, M. Li, H. Huang, H. M. Xu, R. J. Hong and H. Shen, *Optoelectron. Adv. Mater. Rapid Commun.*, 2010, **4**, 1166–1169.

25   Q. Shi, Y. Lei, Y. Wang, H. Wang, L. Jiang, H. Yuan, D. Fang, B. Wang, N. Wu and Y. Gou, *Curr. Appl. Phys.*, 2015, 1–9.

26   B. Fang, B. A. Pinaud and D. P. Wilkinson, *Electrocatalysis*, , DOI:10.1007/s12678-016-0311-4.

27   Q. Guo, D. Zhao, S. Liu, S. Chen, M. Hanif and H. Hou, *Electrochim. Acta*, 2014, **138**, 318–324.

28   G. An and H. Ahn, 2013, **707**, 74–77.

29   R. Padmavathi and D. Sangeetha, *Electrochim. Acta*, 2013, **112**, 1–13.

30   D. Shin, B. Jeong, B. S. Mun, H. Jeon, H. J. Shin, J. Baik and J. Lee, *J. Phys. Chem. C*, 2013, **117**, 11619–11624.

31   R. S. Zhong, Y. H. Qin, D. F. Niu, X. S. Zhang, X. G. Zhou, S. G. Sun and W. K. Yuan, *Electrochim. Acta*, 2013, **89**, 157–162.

32   Z. Lei, L. An, L. Dang, M. Zhao, J. Shi, S. Bai and Y. Cao, *Microporous Mesoporous Mater.*, 2009, **119**, 30–38.

33   G. Zhao, J. He, C. Zhang, J. Zhou, X. Chen and T. Wang, *J. Phys. Chem. C*, 2008, **112**, 1028–1033.

34   D. Yang, S. Chaudhari, K. P. Rajesh and J. Yu, 2014, 1236–1244.

35   J. Yin, Y. Qiu and J. Yu, *J. Electroanal. Chem.*, 2013, **702**, 56–59.

36   F. Alcaide, G. Álvarez, O. Miguel, M. J. Lázaro, R. Moliner, A. López-Cudero, J. Solla-Gullón, E. Herrero and A. Aldaz, *Electrochem. commun.*, 2009, **11**, 1081–1084.

37   Y. Shao, J. Liu, Y. Wang and Y. Lin, *J. Mater. Chem.*, 2009, **19**, 46–59.

38   S. Sharma and B. G. Pollet, *J. Power Sources*, 2012, **208**, 96–119.

39   J. S. Yu, S. Kang, S. B. Yoon and G. Chai, *J. Am. Chem. Soc.*, 2002, **124**, 9382–9383.

40   G. S. Chai, S. B. Yoon, J. Yu, J. Choi and Y. Sung, 2004, 7074–7079.

41   F. B. Su, J. H. Zeng, X. Y. Bao, Y. S. Yu, J. Y. Lee and X. S. Zhao, *Chem. Mater.*, 2005, **17**, 3960–3967.

42   J. Zhu, J. Zhou, T. Zhao, X. Zhou, D. Chen and W. Yuan, *Appl. Catal. A Gen.*, 2009, **352**, 243–250.

43   W. Xu and S. Tao, *J. Mater. Chem. A Mater. energy Sustain.*, 2016, **4**, 16272–16287.

44   C. Te Hung, Z. H. Liou, P. Veerakumar, P. H. Wu, T. C. Liu and S. Bin Liu, *Cuihua Xuebao/Chinese J. Catal.*, 2016, **37**, 43–53.

45   Y. Mao, H. Duan, B. Xu, L. Zhang, Y. Hu, C. Zhao, Z. Wang, L. Chen and Y. Yang, *Energy Environ. Sci.*, 2012, **5**, 7950.

46   L. Zou, Y. Qiao, Z. Y. Wu, X. S. Wu, J. Le Xie, S. H. Yu, J. Guo and C. M. Li, *Adv. Energy Mater.*, 2016, **6**, 1–6.

47   Z. Liu, D. Fu, F. Liu, G. Han, C. Liu, Y. Chang, Y. Xiao, M. Li and S. Li, *Carbon N. Y.*, 2014, **70**, 295–307.

48   X. Zhang, J. He, T. Wang, M. Liu, H. Xue and H. Guo, *J. Mater. Chem. A*, 2014, **2**, 3072.

49   L. Feng, X. Chen, Y. Cao, Y. Chen, F. Wang, Y. Chen and Y. Liu, *RSC Adv.*, 2017, **7**, 14669–14677.

50   R. Brandiele, C. Durante, E. Grądzka, G. A. Rizzi, J. Zheng, D. Badocco, P. Centomo, P. Pastore, G. Granozzi and A. Gennaro, *J. Mater. Chem. A*, 2016, **4**, 12232–12240.

51   X. Bo, L. Zhu, G. Wang and L. Guo, *J. Mater. Chem.*, 2012, **22**, 5758.

52   W. Xu, Z. Wu and S. Tao, *J. Mater. Chem. A*, 2016, **4**, 16272–16287.

53   J. Y. Cheon, C. Ahn, D. J. You, C. Pak, S. H. Hur, J. Kim and S.

54   H. Joo, *J. Mater. Chem. A*, 2013, **1**, 1270–1283.

54   L. Zhang, A. Aboagye, A. Kelkar, C. Lai and H. Fong, *J. Mater. Sci.*, 2014, **49**, 463–480.

55   F. Miao, C. Shao, X. Li, N. Lu, K. Wang, X. Zhang and Y. Liu, *Energy*, 2016, **95**, 233–241.

56   G. Hu, Z. Zhou, Y. Guo, H. Hou and S. Shao, *Electrochem. commun.*, 2010, **12**, 422–426.

57   M. Zhi, S. Liu, Z. Hong and N. Wu, *RSC Adv.*, 2014, **4**, 43619–43623.

58   K. K. Karthikeyan and P. Biji, *Microporous Mesoporous Mater.*, 2016, **224**, 372–383.

59   P. Kanninen, M. Borghei, V. Ruiz, E. I. Kauppinen and T. Kallio, *Int. J. Hydrogen Energy*, 2012, **37**, 19082–19091.

60   Y. H. Kwok, A. C. H. Tsang, Y. Wang and D. Y. C. Leung, *J. Power Sources*, 2017, **349**, 75–83.

61   L. Ren and Y. Xing, *Electrochim. Acta*, 2008, **53**, 5563–5568.

62   S. Sun, G. Zhang, Y. Zhong, H. Liu, R. Li, X. Zhou and X. Sun, *Chem. Commun.*, 2009, 7048.

63   Y. Chen, J. Wang, H. Liu, M. N. Banis, R. Li, X. Sun, T. K. Sham, S. Ye and S. Knights, *J. Phys. Chem. C*, 2011, **115**, 3769–3776.

64   Y. Wang, J. Jin, S. Yang, G. Li and J. Jiang, *Int. J. Hydrogen Energy*, 2016, 1–11.

65   J.-S. Zheng, X.-Z. Wang, R. Fu, D.-J. Yang, P. Li, H. Lv and J.-X. Ma, *Int. J. Hydrogen Energy*, 2012, **37**, 4639–4647.

66   D. Sebastián, C. Alegre, M. E. Gálvez, R. Moliner, M. J. Lázaro, A. S. Aricò and V. Baglio, *J. Mater. Chem. A*, 2014, **2**, 13713.

67   S. Abdulla, T. L. Mathew and B. Pullithadathil, *Sensors Actuators, B Chem.*, 2015, **221**, 1523–1534.

68   B. Singh, E. Dempsey, C. Dickinson and F. Laffir, *Analyst*, 2012, **137**, 1639.

69   B. P. Vinayan, R. Nagar, N. Rajalakshmi and S. Ramaprabhu, *Adv. Funct. Mater.*, 2012, **22**, 3519–3526.

70   D. He, D. Jiang, H. Lv, M. Pan and S. Mu, *Appl. Catal. B Environ.*, 2013, **132**–**133**, 379–388.

71   Z. Li, Q. Gao, H. Zhang, W. Tian, Y. Tan, W. Qian and Z. Liu, *Sci. Rep.*, 2017, **7**, 43352.

72   D. S. Yang, S. Chaudhari, K. P. Rajesh and J. S. Yu, *ChemCatChem*, 2014, **6**, 1236–1244.

73   Z. Zhou, C. Lai, L. Zhang, Y. Qian, H. Hou, D. H. Reneker and H. Fong, *Polymer (Guildf).*, 2009, **50**, 2999–3006.

74   Z. Lei, L. An, L. Dang, M. Zhao, J. Shi, S. Bai and Y. Cao, *Microporous Mesoporous Mater.*, 2009, **119**, 30–38.

75   H. Liu, Z. Shi, J. Zhang, L. Zhang and J. Zhang, *J. Mater. Chem.*, 2009, **19**, 468.

76   J. Song, G. Li and J. Qiao, *Electrochim. Acta*, , DOI:10.1016/j.electacta.2015.03.142.

77   K. Wang, Q. Meng, Y. Zhang, Z. Wei and M. Miao, *Adv. Mater.*, 2013, **25**, 1494–1498.

78   Y. S. Lim, Y. P. Tan, H. N. Lim, N. M. Huang, W. T. Tan, M. A. Yarmo and C. Y. Yin, *Ceram. Int.*, 2014, **40**, 3855–3864.

79   C. R. Bradbury, J. Zhao and D. J. Fermín, *J. Phys. Chem. C*, 2008, **112**, 10153–10160.

80   A. M. Zainoodin, S. K. Kamarudin, M. S. Masdar, W. R. W. Daud, A. B. Mohamad and J. Sahari, *Appl. Energy*, 2014, **113**, 946–954.

39x19mm (300 x 300 DPI)